Draft version December 13, 2022
Typeset using LaTeX **twocolumn** style in AASTeX631

First Look at $z > 1$ Bars in the Rest-Frame Near-Infrared with *JWST* Early CEERS Imaging

Yuchen Guo,[1] Shardha Jogee,[1] Steven L. Finkelstein,[1] Zilei Chen,[1] Eden Wise,[1] Micaela B. Bagley,[1] Guillermo Barro,[2] Stijn Wuyts,[3] Dale D. Kocevski,[4] Jeyhan S. Kartaltepe,[5] Elizabeth J. McGrath,[4] Henry C. Ferguson,[6] Bahram Mobasher,[7] Mauro Giavalisco,[8] Ray A. Lucas,[6] Jorge A. Zavala,[9] Jennifer M. Lotz,[10] Norman A. Grogin,[6] Marc Huertas-Company,[11,12,13] Jesús Vega-Ferrero,[11] Nimish P. Hathi,[6] Pablo Arrabal Haro,[14] Mark Dickinson,[14] Anton M. Koekemoer,[6] Casey Papovich,[15,16] Nor Pirzkal,[17] L. Y. Aaron Yung,[18,*] Bren E. Backhaus ,[19] Eric F. Bell,[20] Antonello Calabrò,[21] Nikko J. Cleri,[15,16] Rosemary T. Coogan,[22] M. C. Cooper,[23] Luca Costantin,[24] Darren Croton,[25,26] Kelcey Davis,[27] Alexander de la Vega,[28] Avishai Dekel,[29] Maximilien Franco,[1] Jonathan P. Gardner,[18] Benne W. Holwerda,[30] Taylor A. Hutchison,[18,*] Viraj Pandya,[31,†] Pablo G. Pérez-González,[32] Swara Ravindranath,[6] Caitlin Rose,[5] Jonathan R. Trump,[19] and Weichen Wang[33]

ABSTRACT

Stellar bars are key drivers of secular evolution in galaxies and can be effectively studied using rest-frame near-infrared (NIR) images, which trace the underlying stellar mass and are less impacted by dust and star formation than rest-frame UV or optical images. We leverage the power of *JWST* CEERS NIRCam images to present the first quantitative identification and characterization of stellar bars at $z > 1$ based on rest-frame NIR F444W images of high resolution ($\sim$1.3 kpc at $z \sim 1$–3). We identify stellar bars in these images using quantitative criteria based on ellipse fits. For this pilot study, we present six examples of robustly identified bars at $z > 1$ with spectroscopic redshifts, including the two highest redshift bars at $z \sim 2.136$ and 2.312 quantitatively identified and characterized to date. The stellar bars at $z \sim 1.1$–2.3 presented in our study have projected semi-major axes of ~ 2.9–4.3 kpc and projected ellipticities of ~ 0.41–0.53 in the rest-frame NIR. The barred host galaxies have stellar masses $\sim 1 \times 10^{10}$ to 2×10^{11} $M_\odot$, star formation rates of $\sim$ 21–295 $M_\odot$ yr^{-1}, and several have potential nearby companions. Our finding of bars at $z \sim 1.1$–2.3 demonstrates the early onset of such instabilities and supports simulations where bars form early in massive dynamically cold disks. It also suggests that if these bars at lookback times of 8–10 Gyr survive out to present epochs, bar-driven secular processes may operate over a long time and have a significant impact on some galaxies by $z \sim 0$.

Keywords: galaxies: formation – galaxies: evolution – galaxies: structure – galaxies: high-redshift galaxies: spiral

1. INTRODUCTION

Stellar bars play a central role in the secular evolution of galaxies by efficiently redistributing mass and angular momentum and driving gas inflows into the circumnuclear region through gravitational torques and shocks (e.g., Athanassoula 2002; Athanassoula et al. 2005; Kormendy & Kennicutt 2004; Jogee et al. 2005). Most present-day spirals are barred (e.g., Eskridge et al. 2000; Laurikainen et al. 2004; Marinova & Jogee 2007; Menéndez-Delmestre et al. 2007), including our own Milky Way (Peters 1975; Blitz & Spergel 1991; Binney et al. 1991; Weiland et al. 1994).

Observational evidence in nearby galaxies suggests bars influence their central molecular gas concentrations (e.g., Sakamoto et al. 1999; Jogee et al. 2005), velocity fields of ionized gas (e.g., Regan et al. 1997), star formation (SF) activity (e.g., Hunt & Malkan 1999; Jogee et al. 2005; Masters et al. 2010; George & Subramanian 2021), and central bulges (e.g., Kormendy & Kennicutt 2004; Jogee et al. 2005; Gadotti et al. 2015). The role of bars on AGN is less clear as both simulations (e.g., Combes & Gerin 1985; Athanassoula 1992a) and observations (e.g., Knapen et al. 1995; Buta & Combes 1996; Jogee et al. 2005) show that bar-driven gas inflows tend to stall in the circumnuclear region where the specific angular momentum of the gas is still too high to fuel the AGN (Jogee 2006).

* NASA Postdoctoral Fellow
† Hubble Fellow

The exploration of stellar bars out to early cosmic times is important for understanding the growth and morphological transformation of galaxies, a process which is driven since $z \sim 4$ by gas accretion (e.g., Katz et al. 2003; Kereš et al. 2005, 2012; Dekel & Birnboim 2006; Faucher-Giguère & Kereš 2011), galaxy mergers and tidal interactions (e.g., Conselice et al. 2003; Kartaltepe et al. 2007; Jogee et al. 2009; Lotz et al. 2010), as well as bar-driven secular processes. Numerous studies show near-infrared (NIR) images are better tracers than optical images of the stellar mass distribution and structural components of galaxies as the effects of dust extinction and SF are lower in the NIR (e.g., Frogel, Quillen, & Pogge 1996, Suess et al. 2022), and the mass-to-light ratio in the NIR is less sensitive to the ages of the stellar populations (e.g., Schneider 2006). Indeed, the bar fraction in bright spirals at $z \sim 0$ is higher in the NIR (e.g., Marinova & Jogee 2007; Menéndez-Delmestre et al. 2007) than in the optical. However, to date, studies of bars out to $z \sim 1$ have only been able to use the rest-frame optical light traced by *Hubble Space Telescope (HST)* WFPC2, ACS, NICMOS, and WFC3 images.

Early *HST* studies of bars in the rest-frame optical by Elmegreen et al. (2004) and Jogee et al. (2004) presented the first evidence of a significant population of barred galaxies out to $z \sim 1$ (lookback time of ~ 8 Gyr), showing that bars are already in place at early times and implying that bar-driven secular processes can potentially operate over many billions of years if these bars survive to the present day. Results on how the bar fraction varies out to $z \sim 1$ have been mixed: some studies (e.g., Elmegreen et al. 2004; Jogee et al. 2004) do not find a strong decline in the bar fraction out to $z \sim 1$, other studies find a decline by a factor of a few (e.g., Sheth et al. 2008; Melvin et al. 2014), while Cameron et al. (2010) points out that results on the bar fraction depend on the stellar mass range.

The vast majority of *HST* studies have explored bars in the rest-frame optical light out to $z \sim 1.2$ (e.g., Abraham et al. 1999; Elmegreen et al. 2004; Jogee et al. 2004; Sheth et al. 2008; Cameron et al. 2010; Melvin et al. 2014). The study by Simmons et al. (2014) represented a first attempt to push the explorations of bars in the rest-frame optical out to $z \leq 2$, but faced challenges in robustly characterizing bars at $z > 1.5$.

The advent of sensitive, high-resolution NIRCam images from the *James Webb Space Telescope* (*JWST*; Gardner et al. 2006) holds the promise of tremendous advances in the exploration of bars at $z > 1$ and provides us for the first time with high-resolution rest-frame NIR images at $z > 1$. At the same time, new high-resolution cosmological simulations (e.g., Kraljic, Bournaud, & Martig 2012; Scannapieco & Athanassoula 2012; Bonoli et al. 2016; Spinoso et al. 2017; Algorry et al. 2017; Fragkoudi et al. 2021; Rosas-Guevara et al. 2020, 2022; Bi et al. 2022) are probing the growth of bars and their impact on galaxy evolution out to $z \geq 4$.

In this pilot study we conduct the first quantitative exploration of stellar bars at $z > 1$ in high-resolution rest-frame NIR images by analyzing *JWST* NIRCam images in the first epoch of imaging from the Cosmic Evolution Early Release Science Survey (CEERS; Finkelstein et al. 2022). Thanks to the *JWST* F444W images, we can for the first time use high-resolution ($0\farcs16$ corresponding to $\sim$1.3 kpc at $z \sim$ 1–3) rest-frame NIR images to quantitatively identify and characterize bars at $z > 1$. The sample selection is outlined in § 3. In § 4 we describe our methodology to identify and characterize bars based on the application of physically motivated quantitative criteria to ellipse fits. For this pilot study, we present in § 5 six examples of robustly identified bars at $z > 1$ with spectroscopic redshifts, including the two highest redshift bars at $z \sim 2.136$ and 2.312 quantitatively identified and characterized to date. § 6 discusses the implications of our results for the onset and impact of early generations of bars on galaxy evolution.

We stress that this pilot study only presents six examples of robustly identified bars at $z > 1$ in the rest-frame NIR rather than a full census of all observable bars at $z > 1$. In future papers that will incorporate the upcoming additional six CEERS pointings, we will present such a full census of observable bars at $z > 1$, estimate the rest-frame optical and NIR bar fraction, and explore the relationship between bars and galaxy properties (SF, bulges, AGN, and presence of companions) using a control sample of unbarred galaxies.

In this paper we assume the latest *Planck* flat ΛCDM cosmology with H_0 =67.36, Ω_m =0.3153, and Ω_Λ =0.6847 (Planck Collaboration et al. 2020). All magnitudes are in the absolute bolometric system (AB; Oke & Gunn 1983).

2. CEERS OBSERVATIONS AND DATA REDUCTION

CEERS is one of 13 early release science surveys designed to obtain data covering all areas of astronomy early in Cycle 1. In this pilot paper we use the first epoch of CEERS NIRCam imaging, which has four of the planned ten pointings obtained on 21 June 2022, known as CEERS1, CEERS2, CEERS3, and CEERS6. We refer the reader to the CEERS survey (Finkelstein et al. 2022) and data reduction (Bagley et al. 2022) papers for a full description of the CEERS survey and briefly summarize the key aspects here. Data were ob-

tained in each pointing in the short-wavelength (SW) channel F115W, F150W, and F200W filters, and long-wavelength (LW) channel F277W, F356W, F410M, and F444W filters with a typical exposure time of 2835 s per filter in each of three dithers, except for F115W which had longer exposure times. A careful initial reduction of the NIRCam images in all four pointings was performed using version 1.5.3 of the *JWST* Calibration Pipeline[1] with some custom modifications. Version v0.07 of the CEERS data reduction was used in this work. As described in Finkelstein et al. (2022), data were processed through Stages 1 and 2 of the pipeline where reduction steps included detector-level correction, wisp subtraction, removal of *1/f* noise, flat fielding, and masking of bad pixels. This was followed by astrometric correction and co-addition of calibrated detector images onto a common output grid using the drizzle algorithm with an inverse variance map weighting (Casertano et al. 2000; Fruchter & Hook 2002). The RMS of the absolute alignment to *HST* F160W is $\sim$ 12-15 mas and the RMS of the NIRCam-to-NIRCam alignment is $\sim$ 5-10 mas. The output mosaics have pixel scales of $0\farcs03$/pixel. The usable total area covered by these observations is 34.5 arcmin^2. As described in Finkelstein et al. (2022) the CEERS v0.07 photometry catalog was produced by using Source Extractor (Bertin & Arnouts 1996) v2.25.0 in two image mode, with an inverse-variance weighted combination of the PSF-matched F277W and F356W images as the detection image, and photometry measured on all seven bands.

3. SAMPLE SELECTION

For this pilot study we follow the procedure below to identify a sample of galaxies with stellar mass $M_* \geq 10^{10} M_\odot$ at redshifts $1 \leq z \leq 3$ that are in the Multi-wavelength Catalogs for the Extended Groth strip (EGS; Stefanon et al. 2017) for CANDELS (Grogin et al. 2011; Koekemoer et al. 2011) and have CEERS NIRCam imaging.

The redshift range $1 \leq z \leq 3$ was selected for the following reasons. We set an upper limit of $z \leq 3$ so that we can trace the rest-frame NIR light at wavelengths $\lambda \geq 1.1$ microns using the longest-wavelength F444W NIRCam image. We set our lower limit at $z \geq 1$ as most *HST* studies have explored bars in the rest-frame optical light out to $z \sim 1.2$ (see § 1) and the properties of bars at $z > 1$ constitute an uncharted territory of great interest. Additionally, in the redshift range of $z \sim 1$–3, the empirically measured point spread function (PSF) of $0\farcs16$ in the F444W band corresponds to a high spatial resolution of ~ 1.3 kpc.

The sample of galaxies is derived by cross-matching the CEERS v0.07 source catalog (Finkelstein et al. 2022) with the CANDELS EGS catalog (Stefanon et al. 2017) within $0\farcs25$, and identifying galaxies with stellar mass $M_* \geq 10^{10} M_\odot$ at redshifts $1 \leq z \leq 3$. At $z \sim 2$, the 90% stellar mass completeness of the CANDELS EGS catalog is $\sim 10^{10} M_\odot$ (Stefanon et al. 2017). This cross-matching results in a sample of 348 galaxies with stellar mass $M_* \geq 10^{10} M_\odot$ at redshifts $1 \leq z \leq 3$.

We use the robust photometric redshifts and stellar mass measurements in the value-added catalogs associated with the CANDELS EGS catalogs (Stefanon et al. 2017). For $\sim$ 67% of the sample, we supplement photometric redshifts with available published spectroscopic redshifts in EGS (N. Hathi 2022, private communication). If a source has more than one spectroscopic redshift measurement, we choose the one with the highest quality.

4. METHODOLOGY

4.1. *Identification of Stellar Bars*

Stellar bars are non-axisymmetric, flattened triaxial systems within stellar disks that are made up of families of periodic stellar orbits that conserve the Jacobi integral. The main bar-supporting family of $\mathbf{x}_1$ orbits are elongated along the long-axis of the stellar bar (e.g., Contopoulos & Papayannopoulos 1980; Athanassoula 1992b). Our methodology to identify bars in the *JWST* data consists of two stages outlined below.

Stage 1: The first stage is a liberal visual classification whose goal is to cast as wide a net as possible for systems with elongated structures that may be putative bar candidates, with the idea that subsequent ellipse fits of these candidates would allow us to identify the barred systems. For the visual classification, we visually inspected postage stamps of six NIRCam images (F115W, F150W, F200W, F277W, F356W, and F444W) of our 348 sample galaxies at $1 \leq z \leq 3$ to first remove unresolved systems and very strongly distorted and asymmetric systems. Among the remaining galaxies, we then liberally selected a sample S1 of galaxies that host any elongated structures (in any band) that might even marginally be stellar bars. We ended up with 82 galaxies in sample S1.

Stage 2: The second stage involves using the methodology described in Jogee et al. (2004) and Marinova & Jogee (2007) to identify bars. In brief, this methodology involves ellipse-fitting the tracer images (e.g., Jedrzejewski 1987; Wozniak et al. 1995; Jogee et al. 2002, 2004; Elmegreen et al. 2004; Marinova & Jogee 2007),

[1] jwst-pipeline.readthedocs.io

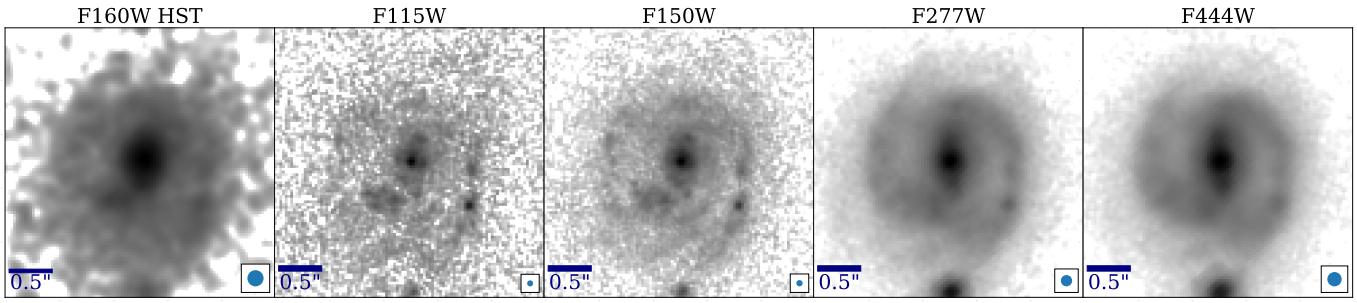

Figure 1. This figure illustrates the effects of bandpass shift and PSF for an example barred galaxy (EGS-23205) at redshift $z \sim 2.136$ in our sample. From left to right, we show the *HST* WFC3 F160W, and *JWST* NIRCam F115W, F150W, F277W, and F444W images. The blue circle at the bottom right of each image represents the point spread function (PSF) FWHM of each band (0.″18, 0.″07, 0.″07, 0.″13, and 0.″16, respectively) and the horizontal bar shows a 0.″5 scale for reference. All images are 3.″0 × 3.″0 in size. The underlying stellar mass distribution and galactic components, such as the stellar bar, are better traced by the high-resolution rest-frame NIR image revealed by the *JWST* F444W data than by the rest-frame UV light shown in the *JWST* F115W images. It is also striking that although the *HST* F160W and *JWST* F444W images have a similar PSF (0.″18 and 0.″16, respectively), the bar is more evident in the JWST image due to the longer rest-frame wavelength light the latter is tracing. Signs of the bar are also visible in the high-resolution rest-frame red optical image traced by the *JWST* F227W data, but are much less evident in the rest-frame blue optical light traced by the *JWST* F150W image. In all images, N is up and E is left.

followed by the application of quantitative criteria to identify bars. For this second stage, we ellipse fitted the F444W image of each galaxy in sample S1. Figure 1 illustrates the effects of bandpass shift and PSF for an example barred galaxy (EGS-23205) at redshift $z \sim 2.136$ in our sample. The stellar bar is evident in the high-resolution rest-frame NIR (*JWST* F444W) image, but not in the rest-frame UV (*JWST* F115W) image. The bar is more evident in the rest-frame NIR *JWST* F444W image than in the rest-frame blue optical *HST* F160W image although the images have a similar PSF (0.″18 and 0.″16, respectively).

Before ellipse-fitting the F444W images of the 82 putative barred galaxies, nearby sources were masked and the pixel values were replaced with interpolated values from the nearby region. Then, the ellipse-fitting was done in two steps:

1. We ran "isophote.Ellipse.fit_image" in PHOTUTILS from Python's astropy package (Bradley et al. 2020) without fixing the center. Doing this step, we let the code fully explore the image and return the center of the ellipse for every ellipse fitted. We then determined the center of isophotes in step 2 by measuring the average center of the ellipses fitted to the inner region.

2. We fixed the center of isophotes at the center measured in step 1 and ran the same routine "isophote.Ellipse.fit_image". During the fitting, the semi-major axis grows geometrically by a factor of 1.1 for each step, and the fitting stops when the relative error in the local radial intensity gradient exceeds 0.5 (Busko 1996) for two consecutive ellipses or the outermost ellipse extends to the region with low signal-to-noise ratio (SNR $\leq$ 3). From the ellipse fits we generate radial profiles of surface brightness (SB), ellipticity (e), and position angle (PA) plotted versus the ellipse semi-major axis a (e.g., see Figures 2 and 3).

In alignment with best practices in the study of bars, we exclude from further consideration of all galaxies with large inclinations ($i > 60°$ as inferred from projected axis ratios of the outer ellipse) as the bar and the outer disk are very hard to separate in such systems. Among the remaining bar candidates, we consider a galaxy to be barred only if it satisfies the two criteria below (e.g., Jogee et al. 2004; Marinova & Jogee 2007):

1. In the bar-dominated region, we require the ellipticity e to rise smoothly to a maximum value $e_{\rm max} > 0.25$, while the PA stays fairly constant along the bar, with some small variation $\Delta\theta_1$ allowed. We discuss the value of $\Delta\theta_1$ later in this section.

2. In the region dominated by the outer disk, we require the ellipticity to drop by at least 0.1 from the bar's maximum ellipticity and the PA to change by at least 10° from the associated bar PA. In galaxies where a transition region exists between the end of the bar and the region dominated by the outer disk, we apply the above criterion to the outer disk region beyond it.

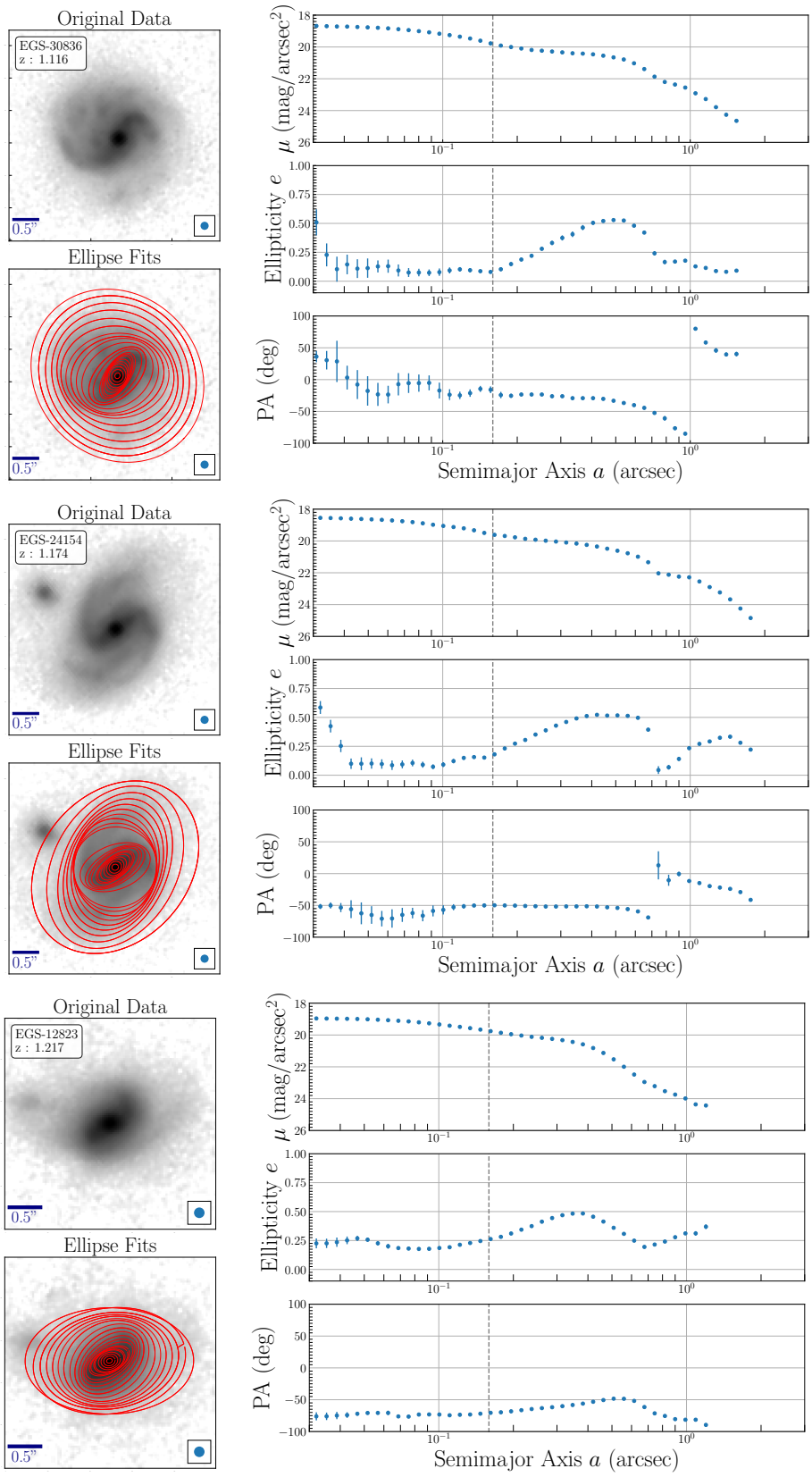

Figure 2. Ellipse fits to the *JWST* NIRCam F444W image of three example barred galaxies (EGS-30836, EGS-24154, EGS-12823). The left panel for each galaxy shows the F444W image alone (top) and then with the ellipse fits superposed (bottom). Although nearby sources may appear in the images, they are masked during the ellipse fitting. The blue circle at the bottom right of each image represents the PSF FWHM (0.″16 corresponding to ∼1.3 kpc at $z \sim 1$–3), and the horizontal bar shows a 0.″5 scale for reference. Size of each image is adjusted with respect to the size of the source, and ranges from 3.″0 × 3.″0 to 3.″9 × 3.″9. The right panel for each galaxy shows the radial profiles of surface brightness (μ), ellipticity (e), and position angle (PA) versus semi-major axis a derived from the ellipse fits. See § 4.1 for details. PA goes from 0 to -90 clockwise (from North to West) and goes from 0 to 90 counter-clockwise (from North to East). The vertical dashed line represents the F444W PSF (0.″16).

We refer the reader to Jogee et al. (2004) and Marinova & Jogee (2007) for a description of the physically motivated justification for the above two criteria for bar identification. We comment here further on the criteria related to the PA. In the first criterion, we required the PA to stay fairly constant along the bar, with some small variation $\Delta\theta_1$ allowed. The rationale for a relatively constant PA is that the main $\mathbf{x}_1$ family of bar-supporting orbits can be modeled by concentric ellipses with a fairly constant PA as a function of semi-major axis in the bar region (Athanassoula 1992b). Many studies do not specify the value they adopt for the allowed variation $\Delta\theta_1$, while others use a wide range in $\Delta\theta_1$ from 20° to 40° (e.g., Jogee et al. 2004; Marinova & Jogee 2007; Olguín-Iglesias et al. 2020). In this pilot paper, we will only show six examples of robustly identified bar candidates where the variation $\Delta\theta_1$ of the PA along the bar is conservatively low at $\Delta\theta_1 \leq 20°$ (see § 5). In our future papers that aim for a more complete census of bars at $z > 1$, we will explore the impact of adopting larger $\Delta\theta_1$ values and fine tuning other aspects of the methodology.

Examples of ellipse fits are shown in Figures 2 and 3 and discussed in the next section. The above two criteria are quite effective in separating barred galaxies from inclined disk galaxies (e.g., see Appendix Figure 5) and unbarred galaxies (e.g., see Appendix Figure 5). We also note that short bars will not be identified in the *JWST* F444W images due to the loss of spatial resolution. We do not expect to robustly identify bars whose semi-major axis is less than the PSF of F444W images (0.″16 corresponding to ∼1.3 kpc at $z \sim 1$–3).

4.2. *Characterization of Bar Length and Maximum Ellipticity*

The shape, length and stellar mass of a stellar bar are important properties that determine the gravitational torque it exerts and its impact on the secular evolution of a galaxy. The main goal of this paper is to identify and demonstrate the existence of bars at $z > 1$, and the ellipse fits presented in the previous section are adequate for this purpose as they robustly identify bars. However, for characterizing the strength, shape, and size of bars, there are more sophisticated methods than ellipse fits and in our future papers we will explore such methods, including generalized ellipses with a shape parameter (Athanassoula et al. 1990; Gadotti 2009a) and multi-component (bulge, bar, outer disk) decomposition of the light distribution (e.g., Laurikainen et al. 2005, 2007; Gadotti 2009b; Weinzirl et al. 2009).

In this paper, we focus on the ellipticity and length of the bar based on ellipse fits. We consider the maximum projected ellipticity of the bar $e_{\rm bar}$ as one measure of bar strength. In the radial profile of projected ellipticity from the ellipse fits (see Figures 2 and 3), the ellipticity rises smoothly to a maximum value in the bar-dominated region and we take this maximum value as $e_{\rm bar}$.

Different definitions of the bar length are used in the bar community, including the following: (i) the semi-major axis (sma) $a_{\rm bar}$ where the bar ellipticity first reaches a maximum value along the bar; (ii) the sma where the bar ellipticity drops steeply or by at least 15% from its maximum value; and (iii) the sma where the PA changes from the bar to the outer disk. In this paper we measure bar lengths based on the first definition as the latter is widely used in many studies (e.g., Athanassoula & Misiriotis 2002; Jogee et al. 2004; Marinova & Jogee 2007; Menéndez-Delmestre et al. 2007) and can be unambiguously applied to many galaxies. However, some studies (e.g., Athanassoula & Misiriotis 2002; Martinez-Valpuesta et al. 2006) suggest this definition can underestimate the true bar length.

5. RESULTS

For this pilot paper, we choose to show six examples of robustly identified barred galaxies that fulfill the following criteria: (i) They have good ellipse fits of the F444W images (Figures 2 and 3), unambiguously meet the two bar criteria in § 4.1, and show a conservatively small variation $\Delta\theta_1 \leq 20°$ in the PA of ellipses fitted along the bar. As we mentioned in § 4.1, the variation $\Delta\theta_1$ allowed for the PA along the bar could in general be higher, but we show the most conservative robust cases of bar here; (ii) The bars have moderate to high maximum projected ellipticities ($e_{\rm bar} \sim 0.41$–0.53) and they are well resolved with projected semi-major axes $a_{\rm bar} \sim 0.″35$–$0.″51$ or ~ 2.9–4.3 kpc (Table 1); (iii) The barred galaxies have a range of published spectroscopic redshifts (N. Hathi 2022, private communication), at $z \sim 1.116$, 1.174, 1.217, 1.543, 2.136, and 2.312 (Table 1), and include the two highest redshift barred galaxies at $z \sim 2.136$ and 2.312, quantitatively identified and characterized to date.

The properties of the six bars and their host galaxies are shown in Figure 4 and Table 1, and the ellipse fits to their F444W images are shown in Figures 2 and 3. In the cases of EGS-30836, EGS-24154, EGS-12823 in Figure 2, as well as EGS-26831, EGS-23205 and EGS-24268 in Figure 3, both bar criteria are well met: the ellipticity rises smoothly to a maximum in the bar-dominated region while the PA stays constant within less than 20°,

Table 1. Barred Galaxies at $z > 1$ in the Rest-Frame NIR from *JWST*

Galaxy Name	$z_{\rm spec}$	$e_{\rm bar}$	$a_{\rm bar}$ (")	$a_{\rm bar}$ (kpc)	$\log(M_\star/M_\odot)$	SFR $M_\odot$ yr^{-1}
(1)	(2)	(3)	(4)	(5)	(6)	(7)
EGS-30836	1.116 (DEEP2 DR4)	~ 0.53	~ 0.51	~ 4.28	10.80	48.430
EGS-24154	1.174 (DEEP2 DR4)	~ 0.52	~ 0.42	~ 3.57	11.05	45.395
EGS-12823	1.217 (3D-HST)	~ 0.48	~ 0.38	~ 3.26	10.63	21.230
EGS-26831	1.543 (MOSDEF)	~ 0.49	~ 0.42	~ 3.65	10.40	74.290
EGS-23205	2.136 (3D-HST)	~ 0.50	~ 0.35	~ 2.95	11.29	295.023
EGS-24268	2.312 (MOSDEF)	~ 0.41	~ 0.35	~ 2.91	10.16	112.808

Note—Columns are: (1) Galaxy ID from Stefanon et al. (2017); (2) Spectroscopic redshift and the survey on which it is based. The 3D-HST redshifts for EGS-12823 and EGS-23205 are based on grism spectra in the 3D-HST Survey (Brammer et al. 2012; Momcheva et al. 2016) and are well constrained. The DEEP2 DR4 and MOSDEF spectroscopic redshifts are from Newman et al. (2013) and Kriek et al. (2015), respectively; (3) The maximum projected ellipticity $e_{\rm bar}$ of the stellar bar in the rest-frame NIR based on *JWST* NIRCam F444W images; (4) As in (3), but for the bar projected semi-major axis $a_{\rm bar}$ in arcsec. (5) As in (3), but for the bar projected semi-major axis $a_{\rm bar}$ in kpc. (6) Stellar mass measurements of the host galaxy from Stefanon et al. (2017); (7) Star-formation rate (SFR) measurements of the host galaxy are the best estimate of the total SFR from the value-added catalogs associated with the CANDELS EGS catalogs (Barro et al. 2019).

and there is a significant drop in ellipticity and change in PA in the region dominated by the outer disk.

To characterize bar properties, we estimated the maximum projected ellipticity ($e_{\rm bar}$) and projected bar length ($a_{\rm bar}$) of the bar for each galaxy with the method described in § 4.2. For our barred galaxies at redshifts of $z \sim 1.1$–2.3, the stellar bar has moderate to high maximum projected ellipticities ($e_{\rm bar}$) in the rest-frame NIR ranging from ~ 0.41 to 0.53 (Table 1). These values overlap with the range of bar projected ellipticities (0.25 to 0.8) seen in NIR images of $z \sim 0$ bright spirals where most ($> 70\%$) bars have $e_{\rm bar} \geq 0.4$ (e.g., Marinova & Jogee 2007; Menéndez-Delmestre et al. 2007). Once we have a larger and more complete sample of bars at $z > 1$, we can evaluate whether the distribution of bar strength and ellipticity evolves down to the present day.

The projected bar length $a_{\rm bar}$ in the rest-frame NIR ranges from ~ 2.9–4.3 kpc with angular sizes of $\sim 0\farcs35$ – $0\farcs51$ (Table 1). For the barred galaxies presented in our study, a typical measurement error due to ellipse fitting of 0.24–0.42 kpc ($0\farcs03$–$0\farcs05$ in angular sizes) on $a_{\rm bar}$ is expected as one cannot measure $a_{\rm bar}$ values better than the step size used in ellipse fitting. The range of $a_{\rm bar}$ values (~ 2.9–4.3 kpc) in these high redshift bars overlaps with the range of stellar bar lengths (1 to 14 kpc) seen in NIR images of $z \sim 0$ bright spirals where most ($> 75\%$) bars have have $a_{\rm bar} \leq 5$ kpc (e.g., Marinova & Jogee 2007). However, as mentioned in § 4.2, we do not expect to robustly identify bars less than the PSF of F444W images ($0\farcs16$ corresponding to $\sim$1.3 kpc at $z \sim 1$–3), so short bars are going to be missed in our study. Additionally, the normalized bar length (ratio of bar length to disk length) is a more meaningful comparison than using the bar length alone, and we will compute the normalized quantities in future papers.

Our six barred galaxies at $z \sim 1.1$–2.3 have published star formation rates (SFRs) ~ 21–$295\ M_\odot$ yr^{-1} (Table 1; Barro et al. 2019). The corresponding specific SFR is $\sim 4 \times 10^{-10}$ to 8×10^{-9} yr^{-1}, indicating these systems are actively star-forming. We stress that this result only applies to the subset of bars we present here and a wider range of specific SFRs may be present in the full bar population.

Our pilot study of barred galaxies at $z > 1$ using high-resolution rest-frame NIR images from *JWST* complements the many past studies that have used *HST* data to explore bars in the rest-frame optical out to $z \sim 1.2$ (e.g., Elmegreen et al. 2004; Jogee et al. 2004; Sheth et al. 2008; Cameron et al. 2010; Melvin et al. 2014) and out to $z \leq 2.0$ (Simmons et al. 2014).

Our study also complements several other recent *JWST* studies that have been submitted or recently

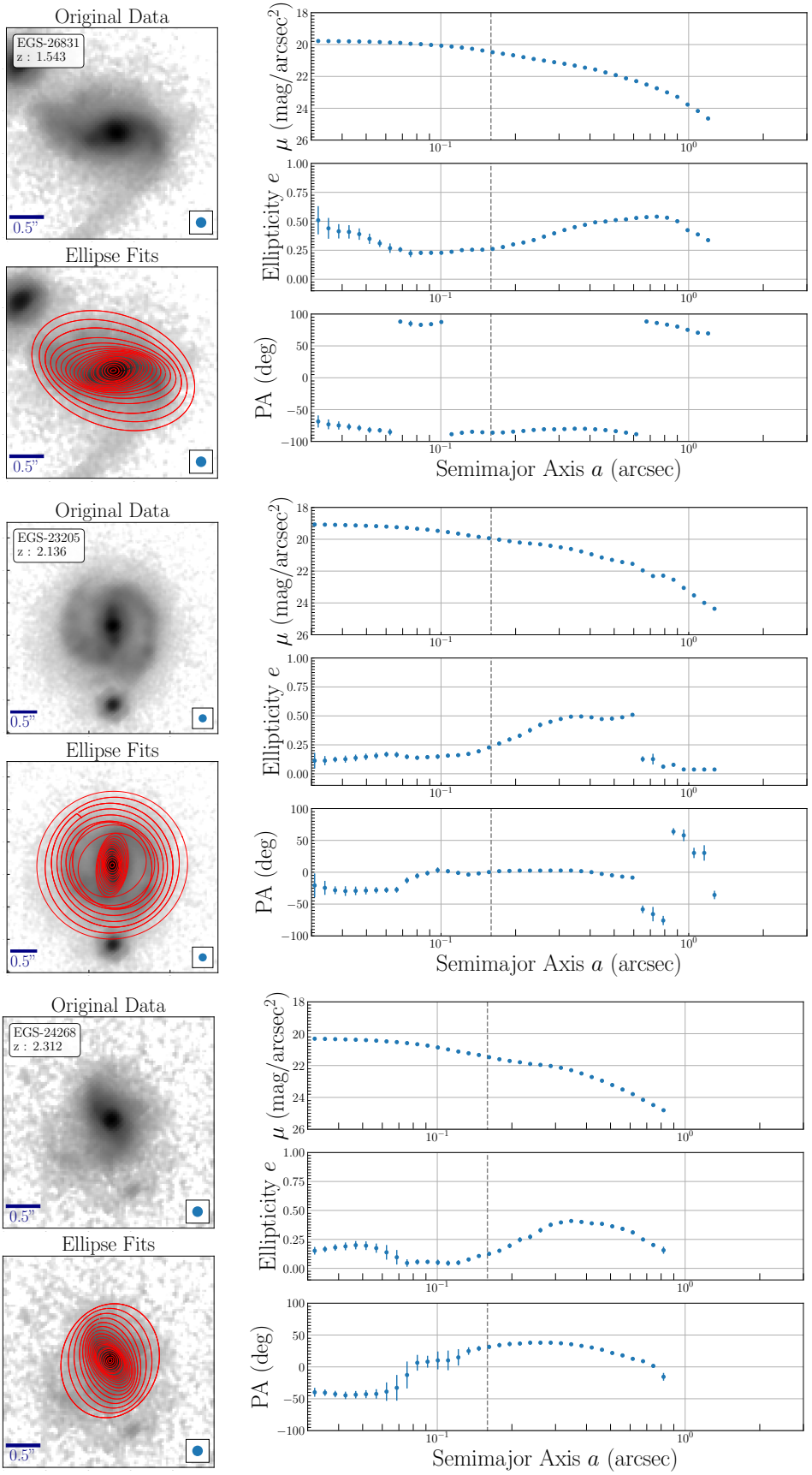

Figure 3. Same as Figure2 for three other example barred galaxies (EGS-26831, EGS-23205, and EGS-24268). See § 4 for details.

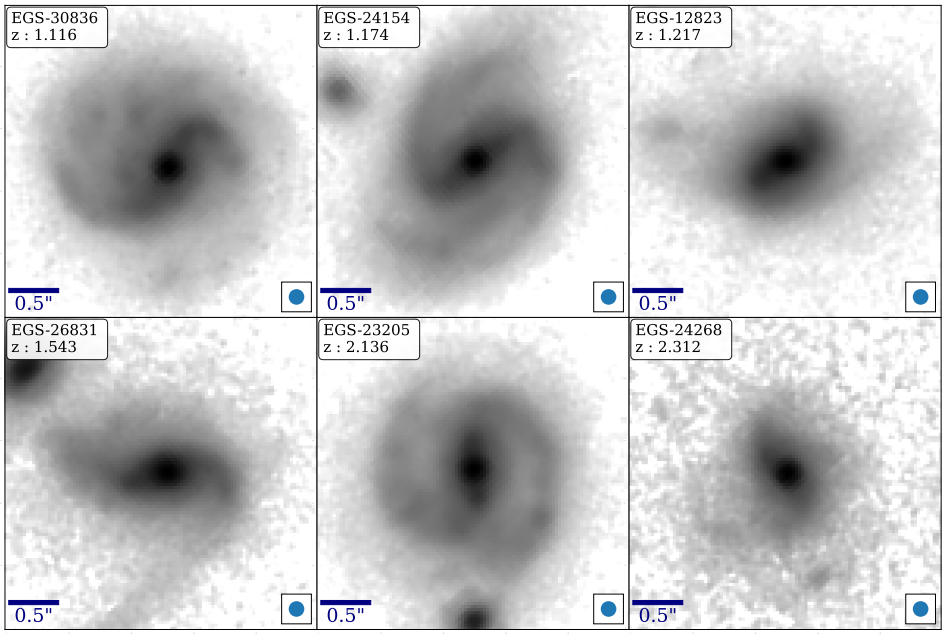

Figure 4. Montage of *JWST* F444W images showing the rest-frame NIR morphology of the six example barred galaxies presented in this paper. The bars were identified by applying quantitative criteria to ellipse fits as outlined in § 4. The labels in the top left of each figure show the CANDELS ID and redshift of each galaxy. The galaxies have spectroscopic redshifts of 1.116 , 1.174, 1.217, 1.543, 2.136, and 2.312 and the last two cases represent the highest redshift bars quantitatively identified and characterized to date. The blue circle at the bottom right of each image represents the point spread function (PSF) FWHM (0.″16 corresponding to ∼1.3 kpc at $z \sim 2$), and the horizontal bar shows a 0.″5 scale for reference. All images are 3.″0 × 3.″0 in size.

accepted for publication. Jacobs et al. (2022) explore the rest-frame optical morphologies of galaxies at $0.8 < z < 5.4$ through visual classification of *JWST* data, mention that "several sources additionally show distinct bars", but provide no further information on the barred galaxies. Chen et al. (2022) performs two-dimensional surface brightness profile fittings of *JWST* images to explore bulges in $z \sim 2$ submillimeter galaxies (Zavala et al. 2017, 2018) and mentions an additional bar component is also needed to improve the fit for EGS-23205 (source 850.025). Finally, Ferreira et al. (2022a) explore morphologies of galaxies at $1.5 < z < 8$ through visual classification of *JWST* images and focus on disks, spheroids, and peculiar galaxies. They mention in some cases, such as our galaxy EGS-23205, "a disk, spiral arms and a bar pops up in the longer wavelength bands", but they do not present a further analysis of the bar. Our study complements the above studies by using quantitative criteria based on ellipse fits of rest-frame *JWST* NIR images to identify bars and to characterize their properties (lengths, ellipticities) and that of their host galaxies. To the best of our knowledge, the two barred galaxies in our pilot study with spectroscopic redshifts $z \sim 2.136$ and $z \sim 2.312$ are the highest redshift bars quantitatively identified and characterized to date.

6. DISCUSSION

When discussing our results, it is important to bear in mind that our pilot study does not present a full census of bars and instead, only highlights six examples of bars at $z > 1$, which have been quantitatively identified and include the two highest-redshift bars at $z \sim 2.136$ and 2.312 known to date. Nonetheless, our present results already allow some interesting conclusions to be drawn and open up exciting possibilities for future work.

Our finding of well developed bars at $z \sim 1.1$–2.3 with projected semi-major axes of ~ 2.9–4.3 kpc and and projected maximum ellipticities of ~ 0.41–0.53 in the rest-frame NIR (§ 5) demonstrates the early onset of such features and supports simulations where bars form early in massive dynamically cold disks (e.g., Bournaud & Combes 2002; Romano-Díaz et al. 2008; Kraljic et al. 2012; Bonoli et al. 2016; Spinoso et al. 2017; Rosas-Guevara et al. 2022; Bi et al. 2022). In a future paper, we will present a census of observable bars at $z > 1$ and estimate the bar fraction in the rest-frame NIR out to $z \sim 3$ using F444W images. These images will detect obscured bars, but the F444W PSF (0.″16 or ∼1.3 kpc at $z \sim 1$–3) will only allow the robust identification of bars with length above 1.3 kpc at $z \sim 1$–3. We will also estimate the rest-frame optical bar fraction out $z \sim 4$ using F200W and other images. While the rest-frame optical

images may miss bars impacted by dust and SF, their smaller PSF (0.″08 or ∼ 650 pc at $z \sim 1$–3) allows them to detect shorter sub-kpc bars, which may constitute a significant fraction of the bars in disk galaxies at early epochs (e.g., Rosas-Guevara et al. 2020, 2022). Recent studies in the rest-frame optical identify a large fraction of disk galaxies at $z \sim 3$ in *JWST* data (e.g., Ferreira et al. 2022b, Kartaltepe et al. 2022).

The topic of the formation, lifetime, and evolution of bars is an area of active research and it depends on the interplay between the stellar disk, dark matter halo, and gaseous components. The properties of the dark matter halo and its exchange of angular momentum with stellar or gaseous components impact the bar (e.g., Athanassoula 2003; Athanassoula, Machado, & Rodionov 2013; Saha & Naab 2013; Sellwood 2016; Collier et al. 2018; Beane et al. 2022). The role of gas is complex. While the presence of a massive and dynamically cold disk of stars and gas favors the onset of $m = 2$ bar instabilities (e.g., Romano-Díaz et al. 2008; Bournaud & Combes 2002; Kraljic et al. 2012; Bonoli et al. 2016; Spinoso et al. 2017; Rosas-Guevara et al. 2022; Bi et al. 2022), gas clumps that sink by dynamical friction can heat the stellar disk (e.g., Shlosman & Noguchi 1993) and large central gaseous mass concentrations can weaken or destroy some bars (e.g., Bournaud & Combes 2002; Shen & Sellwood 2004; Athanassoula et al. 2005; Bournaud et al. 2005; Debattista et al. 2006).

Numerous simulations have also shown that bars can form spontaneously in isolated disks or be tidally induced (e.g., Hernquist & Mihos 1995; Izquierdo-Villalba et al. 2022). In that context, it is interesting to note that many of the six example barred galaxies appear to have nearby sources that could be potential companions. EGS-26831 has a spectroscopic redshift of $z \sim 1.543$ and has two potential companions detected in Stefanon et al. (2017): the source to its northeast (partially visible in Figure 4) has a similar but poorly constrained photometric redshift (Stefanon et al. 2017) within $\Delta z/(1+z) \sim 0.065$ and is at an angular distance of ∼ 1.″62 (corresponding to ∼ 14 kpc assuming for $z \sim 1.543$), while the source to the southeast (not visible in Figure 4) has a poorly constrained photometric redshift (Stefanon et al. 2017) within $\Delta z/(1+z) \sim 0.0056$ and is at an angular distance ∼ 2.″44 (corresponding to ∼ 21 kpc for $z \sim 1.543$). Even though those two sources have poorly constrained photometric redshifts, the interacting features shown in the F444W image suggest that the sources could potentially be companions of EGS-26831. For EGS-24154 whose spectroscopic redshift is $z \sim 1.174$, the source to its northeast (partially visible in Figure 4) is detected in Stefanon et al. (2017) and could be a potential companion as it has a spectroscopic redshift (3D-HST; Brammer et al. 2012; Momcheva et al. 2016) within $\Delta z/(1+z) \sim 0.001$ at an angular distance ∼ 1.″4 (corresponding to ∼ 12 kpc for $z \sim 1.174$). For EGS-23205 at $z \sim 2.136$, the bright source to its south (shown in Figure 4) is identified as an X-ray luminous AGN with an estimated photometric redshift of $z \sim 4.1$ (Kocevski et al. 2022). Given the difficulty of deriving accurate photometric redshifts for luminous AGN, it is unclear how reliable this redshift is and whether the AGN is a chance projection or a true companion. It is also noteworthy that there are faint sources near EGS-30836, EGS-12823 and EGS-24268. Those faint sources are not detected in the CANDELS EGS catalog (Stefanon et al. 2017), so we do not have redshifts to determine whether they are companions, accreted sources or overdensities in the disk. In future papers we will explore the frequency of tidal interactions in a larger sample of barred galaxies and a control sample of unbarred systems.

The growth and rich morphological transformation of galaxies from $z \sim 4$ to today is likely driven by several mechanisms, including bar-driven secular processes (e.g., Sakamoto et al. 1999; Kormendy & Kennicutt 2004; Jogee et al. 2005), galaxy mergers and tidal interactions (e.g., Conselice et al. 2003; Kartaltepe et al. 2007; Jogee et al. 2009; Lotz et al. 2010), and gas accretion (e.g., Katz et al. 2003; Kereš et al. 2005; Dekel & Birnboim 2006; Faucher-Giguère & Kereš 2011; Kereš et al. 2012). Our finding of bars at $z \sim 1.1$–2.3 (lookback times of 8–10 Gyr) also suggests that if these bars survive out to present epochs, bar-driven secular processes may operate over a long time and have a significant impact on some galaxies by $z \sim 0$. In this context, we note that Gadotti et al. (2015) suggest that the bar in the nearby galaxy NGC 4371 has a formation epoch of $z \sim 2$.

Our subset of barred galaxies at at $z \sim 1.1$–2.3 have SFRs ∼ 21–295 $M_\odot$ yr^{-1} and specific SFRs $\sim 4 \times 10^{-10}$ to 8×10^{-9} yr^{-1} and are thus actively forming stars. Bars drive large gas inflows into the circumnuclear regions via gravitational torques and shocks and can lead a phase of high circumnuclear SFR and potentially depressed or quenched SF in the disk (e.g., Hunt & Malkan 1999; Jogee et al. 2005; Masters et al. 2010, 2012; Khoperskov et al. 2018; George & Subramanian 2021). We will explore more fully the impact of bars on galaxy SFRs in a future paper where we will incorporate the upcoming additional CEERS pointings and make a statistical comparison of the SFRs of barred and unbarred systems.

7. SUMMARY

The exploration of stellar bars out to early cosmic times is essential for understanding the evolution of galaxies as bars play a critical role in driving the secular evolution of galaxies. Stellar bars can be effectively mapped in rest-frame NIR images, which trace the underlying stellar mass and are less impacted by dust and star formation than rest-frame UV or optical images. In this pilot study we conduct the first quantitative identification and characterization of stellar bars at $z > 1$ in high-resolution rest-frame NIR images by analyzing *JWST* F444W images in the first epoch of imaging from the CEERS survey. We focus on a sample of 348 galaxies at redshifts $1 \leq z \leq 3$, with stellar mass $M_* \geq 10^{10} M_\odot$ and CANDELS multi-wavelength data.

The *JWST* F444W images allow us achieve a high-resolution ($0\farcs16$ corresponding to ~ 1.3 kpc at $z \sim 1$–3) at rest-frame NIR wavelengths to quantitatively identify and characterize bars at $z > 1$. We identify stellar bars by performing a first-pass visual classification, followed by ellipse fits and the application of physically motivated quantitative criteria to the ellipse fits. For this pilot study we present six examples of robustly identified bars at $z > 1$ with spectroscopic redshifts, including the two highest redshift bars at $z \sim 2.136$ and 2.312, quantitatively identified and characterized to date. Our study complements *HST* studies in the last two decades that have mainly traced bars in the rest-frame optical out to $z \sim 1$.

The examples of stellar bars at $z \sim 1.1$–2.3 presented in our study have projected semi-major axes of ~ 2.9–4.3 kpc and moderate to high projected maximum ellipticities of ~ 0.41–0.53 in the rest-frame NIR, indicating they are already fairly strong and well developed at these early cosmic times. The barred host galaxies have stellar masses $\sim 1 \times 10^{10}$ to 2×10^{11} $M_\odot$, star formation rates of $\sim$ 21–295 $M_\odot$ yr^{-1}, and several have potential nearby companions. Our finding of bars at $z \sim 1.1$–2.3 demonstrates the early onset of such instabilities and supports simulations where bars form early in massive dynamically cold disks. It also suggests that if these bars at lookback times of 8–10 Gyr survive out to present epochs, bar-driven secular processes may operate over a long time and have a significant impact on some galaxies by $z \sim 0$.

This pilot study only presents six examples of robustly identified bars at $z > 1$ in the rest-frame NIR. We do not present here a full census of all observable bars at $z > 1$ and the associated statistical distribution of their properties. In future papers that will incorporate the upcoming additional six CEERS pointings, we will present such a census, estimate the rest-frame optical and NIR bar fraction, and explore the relationship between bars and galaxy properties (SF, bulges, AGN, and presence of companions) using a control sample of unbarred galaxies.

Version v0.07 of the CEERS data reduction was used in this work. The full set of the latest CEERS data products can be found at MAST via https://doi.org/10.17909/z7p0-8481.

We thank the entire *JWST* team, including the engineers for making possible this wonderful over-performing telescope, the commissioning team for obtaining these early data, and the pipeline teams for their work over the years building and supporting the pipeline. YG and SJ acknowledge support from the Roland K. Blumberg Endowment in Astronomy and Heising-Simons Foundation grant 2017-0464. MBB and SLF acknowledge support from NASA through STScI ERS award JWST-ERS-1345. The authors acknowledge the Texas Advanced Computing Center (TACC) at The University of Texas at Austin for providing HPC and visualization resources that have contributed to the research results reported within this paper. URL: http://www.tacc.utexas.edu

Software: Astropy (Astropy Collaboration et al. 2013), Photutils (Bradley et al. 2020), SciPy (Virtanen et al. 2020), Source Extractor (Bertin & Arnouts 1996), STScI *JWST* Calibration Pipeline (jwst-pipeline.readthedocs.io)

REFERENCES

Abraham, R. G., Merrifield, M. R., Ellis, R. S., Tanvir, N. R., & Brinchmann, J. 1999, MNRAS, 308, 569, doi: 10.1046/j.1365-8711.1999.02766.x

Algorry, D. G., Navarro, J. F., Abadi, M. G., et al. 2017, MNRAS, 469, 1054, doi: 10.1093/mnras/stx1008

Astropy Collaboration, Robitaille, T. P., Tollerud, E. J., et al. 2013, A&A, 558, A33, doi: 10.1051/0004-6361/201322068

Athanassoula, E. 1992a, MNRAS, 259, 345, doi: 10.1093/mnras/259.2.345

—. 1992b, MNRAS, 259, 328, doi: 10.1093/mnras/259.2.328

—. 2002, ApJL, 569, L83, doi: 10.1086/340784

—. 2003, MNRAS, 341, 1179, doi: 10.1046/j.1365-8711.2003.06473.x

Athanassoula, E., Lambert, J. C., & Dehnen, W. 2005, MNRAS, 363, 496, doi: 10.1111/j.1365-2966.2005.09445.x

Athanassoula, E., Machado, R. E. G., & Rodionov, S. A. 2013, MNRAS, 429, 1949, doi: 10.1093/mnras/sts452

Athanassoula, E., & Misiriotis, A. 2002, MNRAS, 330, 35, doi: 10.1046/j.1365-8711.2002.05028.x

Athanassoula, E., Morin, S., Wozniak, H., et al. 1990, MNRAS, 245, 130

Bagley, M. B., Finkelstein, S. L., Koekemoer, A. M., et al. 2022, arXiv e-prints, arXiv:2211.02495. https://arxiv.org/abs/2211.02495

Barro, G., Pérez-González, P. G., Cava, A., et al. 2019, ApJS, 243, 22, doi: 10.3847/1538-4365/ab23f2

Beane, A., Hernquist, L., D'Onghia, E., et al. 2022, arXiv e-prints, arXiv:2209.03364. https://arxiv.org/abs/2209.03364

Bertin, E., & Arnouts, S. 1996, A&AS, 117, 393

Bi, D., Shlosman, I., & Romano-Díaz, E. 2022, ApJ, 934, 52, doi: 10.3847/1538-4357/ac779b

Binney, J., Gerhard, O. E., Stark, A. A., Bally, J., & Uchida, K. I. 1991, MNRAS, 252, 210, doi: 10.1093/mnras/252.2.210

Blitz, L., & Spergel, D. N. 1991, ApJ, 379, 631, doi: 10.1086/170535

Bonoli, S., Mayer, L., Kazantzidis, S., et al. 2016, MNRAS, 459, 2603, doi: 10.1093/mnras/stw694

Bournaud, F., & Combes, F. 2002, A&A, 392, 83, doi: 10.1051/0004-6361:20020920

Bournaud, F., Combes, F., & Semelin, B. 2005, MNRAS, 364, L18, doi: 10.1111/j.1745-3933.2005.00096.x

Bradley, L., Sipőcz, B., Robitaille, T., et al. 2020, astropy/photutils: 1.0.0, 1.0.0, Zenodo, Zenodo, doi: 10.5281/zenodo.4044744

Brammer, G. B., van Dokkum, P. G., Franx, M., et al. 2012, ApJS, 200, 13, doi: 10.1088/0067-0049/200/2/13

Busko, I. C. 1996, in Astronomical Society of the Pacific Conference Series, Vol. 101, Astronomical Data Analysis Software and Systems V, ed. G. H. Jacoby & J. Barnes, 139

Buta, R., & Combes, F. 1996, FCPh, 17, 95

Cameron, E., Carollo, C. M., Oesch, P., et al. 2010, MNRAS, 409, 346, doi: 10.1111/j.1365-2966.2010.17314.x

Casertano, S., de Mello, D., Dickinson, M., et al. 2000, AJ, 120, 2747, doi: 10.1086/316851

Chen, C.-C., Gao, Z.-K., Hsu, Q.-N., et al. 2022, ApJL, 939, L7, doi: 10.3847/2041-8213/ac98c6

Collier, A., Shlosman, I., & Heller, C. 2018, MNRAS, 476, 1331, doi: 10.1093/mnras/sty270

Combes, F., & Gerin, M. 1985, A&A, 150, 327

Conselice, C. J., Bershady, M. A., Dickinson, M., & Papovich, C. 2003, AJ, 126, 1183, doi: 10.1086/377318

Contopoulos, G., & Papayannopoulos, T. 1980, A&A, 92, 33

Debattista, V. P., Mayer, L., Carollo, C. M., et al. 2006, ApJ, 645, 209, doi: 10.1086/504147

Dekel, A., & Birnboim, Y. 2006, MNRAS, 368, 2, doi: 10.1111/j.1365-2966.2006.10145.x

Elmegreen, B. G., Elmegreen, D. M., & Hirst, A. C. 2004, ApJ, 612, 191, doi: 10.1086/422407

Eskridge, P. B., Frogel, J. A., Pogge, R. W., et al. 2000, AJ, 119, 536, doi: 10.1086/301203

Faucher-Giguère, C.-A., & Kereš, D. 2011, MNRAS, 412, L118, doi: 10.1111/j.1745-3933.2011.01018.x

Ferreira, L., Conselice, C. J., Sazonova, E., et al. 2022a, arXiv e-prints, arXiv:2210.01110. https://arxiv.org/abs/2210.01110

Ferreira, L., Adams, N., Conselice, C. J., et al. 2022b, ApJL, 938, L2, doi: 10.3847/2041-8213/ac947c

Finkelstein, S. L., Bagley, M. B., Arrabal Haro, P., et al. 2022, arXiv e-prints, arXiv:2207.12474. https://arxiv.org/abs/2207.12474

Fragkoudi, F., Grand, R. J. J., Pakmor, R., et al. 2021, A&A, 650, L16, doi: 10.1051/0004-6361/202140320

Frogel, J. A., Quillen, A. C., & Pogge, R. W. 1996, in New Extragalactic Perspectives in the New South Africa, ed. D. L. Block & J. M. Greenberg (Dordrecht: Springer Netherlands), 65–83

Fruchter, A. S., & Hook, R. N. 2002, PASP, 114, 144, doi: 10.1086/338393

Gadotti, D. A. 2009a, in Astrophysics and Space Science Proceedings, Vol. 8, Chaos in Astronomy, 159, doi: 10.1007/978-3-540-75826-6_15

Gadotti, D. A. 2009b, MNRAS, 393, 1531, doi: 10.1111/j.1365-2966.2008.14257.x

Gadotti, D. A., Seidel, M. K., Sánchez-Blázquez, P., et al. 2015, A&A, 584, A90, doi: 10.1051/0004-6361/201526677

Gardner, J. P., Mather, J. C., Clampin, M., et al. 2006, SSRv, 123, 485, doi: 10.1007/s11214-006-8315-7

George, K., & Subramanian, S. 2021, A&A, 651, A107, doi: 10.1051/0004-6361/202140697

Grogin, N. A., Kocevski, D. D., Faber, S. M., et al. 2011, ApJS, 197, 35, doi: 10.1088/0067-0049/197/2/35

Hernquist, L., & Mihos, J. C. 1995, ApJ, 448, 41, doi: 10.1086/175940

Hunt, L. K., & Malkan, M. A. 1999, ApJ, 516, 660, doi: 10.1086/307150

Izquierdo-Villalba, D., Bonoli, S., Rosas-Guevara, Y., et al. 2022, MNRAS, 514, 1006, doi: 10.1093/mnras/stac1413

Jacobs, C., Glazebrook, K., Calabrò, A., et al. 2022, arXiv e-prints, arXiv:2208.06516. https://arxiv.org/abs/2208.06516

Jedrzejewski, R. I. 1987, MNRAS, 226, 747, doi: 10.1093/mnras/226.4.747

Jogee, S. 2006, in Physics of Active Galactic Nuclei at all Scales, ed. D. Alloin, Vol. 693, 143, doi: 10.1007/3-540-34621-X_6

Jogee, S., Knapen, J. H., Laine, S., et al. 2002, ApJL, 570, L55, doi: 10.1086/340974

Jogee, S., Scoville, N., & Kenney, J. D. P. 2005, ApJ, 630, 837, doi: 10.1086/432106

Jogee, S., Barazza, F. D., Rix, H.-W., et al. 2004, ApJL, 615, L105, doi: 10.1086/426138

Jogee, S., Miller, S. H., Penner, K., et al. 2009, ApJ, 697, 1971, doi: 10.1088/0004-637X/697/2/1971

Kartaltepe, J. S., Sanders, D. B., Scoville, N. Z., et al. 2007, ApJS, 172, 320, doi: 10.1086/519953

Kartaltepe, J. S., Rose, C., Vanderhoof, B. N., et al. 2022, arXiv e-prints, arXiv:2210.14713. https://arxiv.org/abs/2210.14713

Katz, N., Keres, D., Dave, R., & Weinberg, D. H. 2003, in Astrophysics and Space Science Library, Vol. 281, The IGM/Galaxy Connection. The Distribution of Baryons at z=0, ed. J. L. Rosenberg & M. E. Putman, 185, doi: 10.1007/978-94-010-0115-1_34

Kereš, D., Katz, N., Weinberg, D. H., & Davé, R. 2005, MNRAS, 363, 2, doi: 10.1111/j.1365-2966.2005.09451.x

Kereš, D., Vogelsberger, M., Sijacki, D., Springel, V., & Hernquist, L. 2012, MNRAS, 425, 2027, doi: 10.1111/j.1365-2966.2012.21548.x

Khoperskov, S., Di Matteo, P., Gerhard, O., et al. 2018, arXiv e-prints, arXiv:1811.09205. https://arxiv.org/abs/1811.09205

Knapen, J. H., Beckman, J. E., Heller, C. H., Shlosman, I., & de Jong, R. S. 1995, ApJ, 454, 623, doi: 10.1086/176516

Kocevski, D. D., Barro, G., McGrath, E. J., et al. 2022, arXiv e-prints, arXiv:2208.14480. https://arxiv.org/abs/2208.14480

Koekemoer, A. M., Faber, S. M., Ferguson, H. C., et al. 2011, ApJS, 197, 36, doi: 10.1088/0067-0049/197/2/36

Kormendy, J., & Kennicutt, Robert C., J. 2004, ARA&A, 42, 603, doi: 10.1146/annurev.astro.42.053102.134024

Kraljic, K., Bournaud, F., & Martig, M. 2012, ApJ, 757, 60, doi: 10.1088/0004-637X/757/1/60

Kriek, M., Shapley, A. E., Reddy, N. A., et al. 2015, ApJS, 218, 15, doi: 10.1088/0067-0049/218/2/15

Laurikainen, E., Salo, H., & Buta, R. 2004, ApJ, 607, 103, doi: 10.1086/383462

—. 2005, MNRAS, 362, 1319, doi: 10.1111/j.1365-2966.2005.09404.x

Laurikainen, E., Salo, H., Buta, R., & Knapen, J. H. 2007, MNRAS, 381, 401, doi: 10.1111/j.1365-2966.2007.12299.x

Lotz, J. M., Jonsson, P., Cox, T. J., & Primack, J. R. 2010, MNRAS, 404, 590, doi: 10.1111/j.1365-2966.2010.16269.x

Marinova, I., & Jogee, S. 2007, ApJ, 659, 1176, doi: 10.1086/512355

Martinez-Valpuesta, I., Shlosman, I., & Heller, C. 2006, ApJ, 637, 214, doi: 10.1086/498338

Masters, K. L., Mosleh, M., Romer, A. K., et al. 2010, MNRAS, 405, 783, doi: 10.1111/j.1365-2966.2010.16503.x

Masters, K. L., Nichol, R. C., Haynes, M. P., et al. 2012, MNRAS, 424, 2180, doi: 10.1111/j.1365-2966.2012.21377.x

Melvin, T., Masters, K., Lintott, C., et al. 2014, MNRAS, 438, 2882, doi: 10.1093/mnras/stt2397

Menéndez-Delmestre, K., Sheth, K., Schinnerer, E., Jarrett, T. H., & Scoville, N. Z. 2007, ApJ, 657, 790, doi: 10.1086/511025

Momcheva, I. G., Brammer, G. B., van Dokkum, P. G., et al. 2016, ApJS, 225, 27, doi: 10.3847/0067-0049/225/2/27

Newman, J. A., Cooper, M. C., Davis, M., et al. 2013, ApJS, 208, 5, doi: 10.1088/0067-0049/208/1/5

Oke, J. B., & Gunn, J. E. 1983, ApJ, 266, 713

Olguín-Iglesias, A., Kotilainen, J., & Chavushyan, V. 2020, MNRAS, 492, 1450, doi: 10.1093/mnras/stz3549

Peters, W. L., I. 1975, ApJ, 195, 617, doi: 10.1086/153363

Planck Collaboration, Aghanim, N., Akrami, Y., et al. 2020, A&A, 641, A6, doi: 10.1051/0004-6361/201833910

Regan, M. W., Vogel, S. N., & Teuben, P. J. 1997, ApJL, 482, L143, doi: 10.1086/310717

Romano-Díaz, E., Shlosman, I., Heller, C., & Hoffman, Y. 2008, ApJL, 687, L13, doi: 10.1086/593168
Rosas-Guevara, Y., Bonoli, S., Dotti, M., et al. 2020, MNRAS, 491, 2547, doi: 10.1093/mnras/stz3180
—. 2022, MNRAS, 512, 5339, doi: 10.1093/mnras/stac816
Saha, K., & Naab, T. 2013, MNRAS, 434, 1287, doi: 10.1093/mnras/stt1088
Sakamoto, K., Okumura, S. K., Ishizuki, S., & Scoville, N. Z. 1999, ApJ, 525, 691, doi: 10.1086/307910
Scannapieco, C., & Athanassoula, E. 2012, MNRAS, 425, L10, doi: 10.1111/j.1745-3933.2012.01291.x
Schneider, P. 2006, Extragalactic Astronomy and Cosmology
Sellwood, J. A. 2016, ApJ, 819, 92, doi: 10.3847/0004-637X/819/2/92
Shen, J., & Sellwood, J. A. 2004, ApJ, 604, 614, doi: 10.1086/382124
Sheth, K., Elmegreen, D. M., Elmegreen, B. G., et al. 2008, ApJ, 675, 1141, doi: 10.1086/524980
Shlosman, I., & Noguchi, M. 1993, ApJ, 414, 474, doi: 10.1086/173094
Simmons, B. D., Melvin, T., Lintott, C., et al. 2014, MNRAS, 445, 3466, doi: 10.1093/mnras/stu1817
Spinoso, D., Bonoli, S., Dotti, M., et al. 2017, MNRAS, 465, 3729, doi: 10.1093/mnras/stw2934
Stefanon, M., Yan, H., Mobasher, B., et al. 2017, ApJS, 229, 32, doi: 10.3847/1538-4365/aa66cb
Suess, K. A., Bezanson, R., Nelson, E. J., et al. 2022, ApJL, 937, L33, doi: 10.3847/2041-8213/ac8e06
Virtanen, P., Gommers, R., Oliphant, T. E., et al. 2020, Nature Methods, 17, 261, doi: 10.1038/s41592-019-0686-2
Weiland, J. L., Arendt, R. G., Berriman, G. B., et al. 1994, ApJL, 425, L81, doi: 10.1086/187315
Weinzirl, T., Jogee, S., Khochfar, S., Burkert, A., & Kormendy, J. 2009, ApJ, 696, 411, doi: 10.1088/0004-637X/696/1/411
Wozniak, H., Friedli, D., Martinet, L., Martin, P., & Bratschi, P. 1995, A&AS, 111, 115
Zavala, J. A., Aretxaga, I., Geach, J. E., et al. 2017, MNRAS, 464, 3369, doi: 10.1093/mnras/stw2630
Zavala, J. A., Aretxaga, I., Dunlop, J. S., et al. 2018, MNRAS, 475, 5585, doi: 10.1093/mnras/sty217

APPENDIX

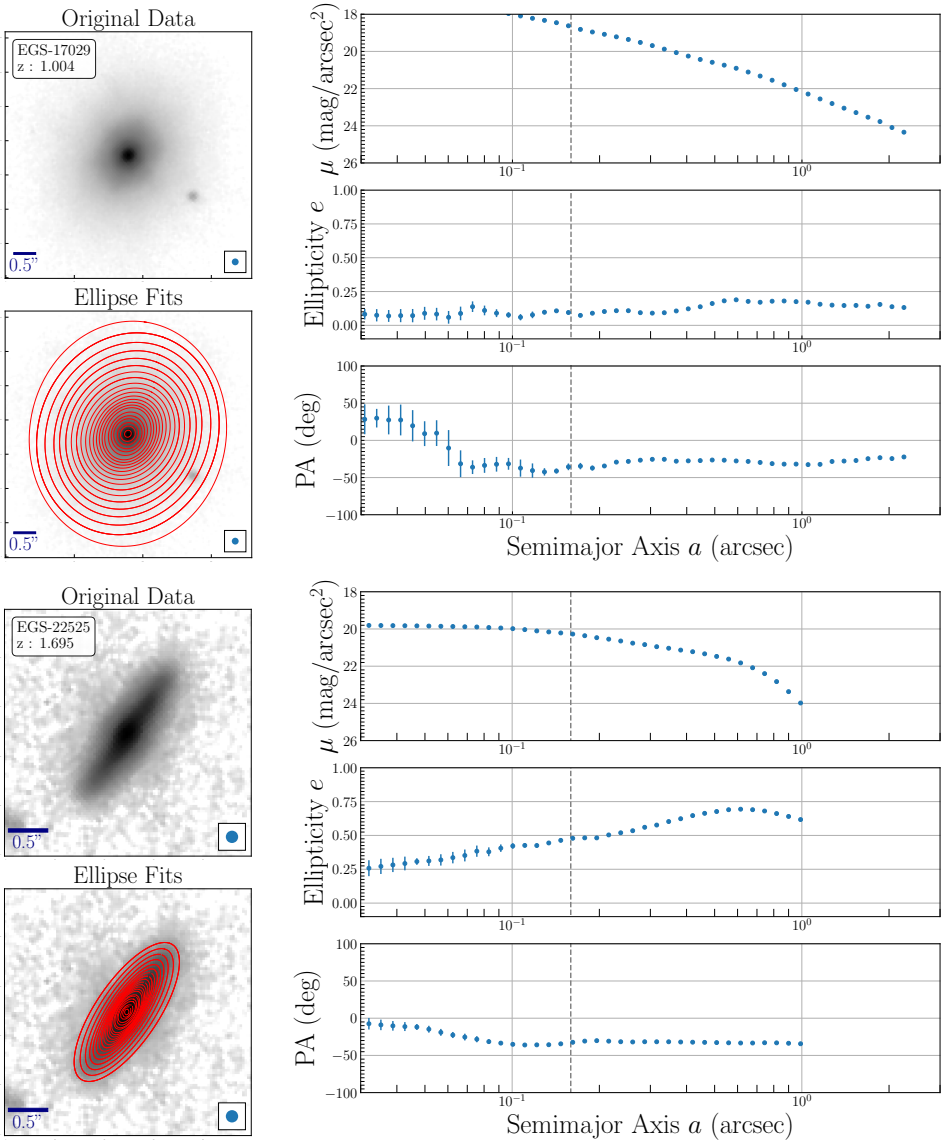

Figure 5. Ellipse fits to the *JWST* NIRCam F444W image of an unbarred face-on disk galaxy (EGS-17029) and an inclined disk galaxy (EGS-22525). The left panel for each galaxy shows the F444W image alone (top) and then with the ellipse fits superposed (bottom). The blue circle at the bottom right of each image represents the PSF FWHM (0.″16 corresponding to ∼ 1.3 kpc at $z \sim$ 1-3), and the horizontal bar shows a 0.″5 scale for reference. Size of each image is adjusted with respect to the size of the source, and ranges from 4.″5 × 4.″5 to 3.″0 × 3.″0. The right panel for each galaxy shows the radial profiles of surface brightness (μ), ellipticity (e), and position angle (PA) versus semi-major axis a derived from the ellipse fits. The vertical dashed line represents the F444W PSF (0.″16). The profiles do not show the characteristic bar signatures that meet our criteria in § 4.1.

All Authors and Affiliations

Yuchen Guo,[1] Shardha Jogee,[1] Steven L. Finkelstein,[1] Zilei Chen,[1] Eden Wise,[1] Micaela B. Bagley,[1] Guillermo Barro,[2] Stijn Wuyts,[3] Dale D. Kocevski,[4] Jeyhan S. Kartaltepe,[5] Elizabeth J. McGrath,[4] Henry C. Ferguson,[6] Bahram Mobasher,[7] Mauro Giavalisco,[8] Ray A. Lucas,[6] Jorge A. Zavala,[9] Jennifer M. Lotz,[10] Norman A. Grogin,[6] Marc Huertas-Company,[11,12,13] Jesús Vega-Ferrero,[11] Nimish P. Hathi,[6] Pablo Arrabal Haro,[14] Mark Dickinson,[14] Anton M. Koekemoer,[6] Casey Papovich,[15,16] Nor Pirzkal,[17] L. Y. Aaron Yung,[18,*] Bren E. Backhaus ,[19] Eric F. Bell,[20] Antonello Calabrò,[21] Nikko J. Cleri,[15,16] Rosemary T. Coogan,[22] M. C. Cooper,[23] Luca Costantin,[24] Darren Croton,[25,26] Kelcey Davis,[27] Alexander de la Vega,[28] Avishai Dekel,[29] Maximilien Franco,[1] Jonathan P. Gardner,[18] Benne W. Holwerda,[30] Taylor A. Hutchison,[18,*] Viraj Pandya,[31,†] Pablo G. Pérez-González,[32] Swara Ravindranath,[6] Caitlin Rose,[5] Jonathan R. Trump,[19] and Weichen Wang[33]

[1] *Department of Astronomy, The University of Texas at Austin, Austin, TX, USA*

[2] *Department of Physics, University of the Pacific, Stockton, CA 90340 USA*

[3] *Department of Physics, University of Bath, Claverton Down, Bath BA2 7AY, UK*

[4] *Department of Physics and Astronomy, Colby College, Waterville, ME 04901, USA*

[5] *Laboratory for Multiwavelength Astrophysics, School of Physics and Astronomy, Rochester Institute of Technology, 84 Lomb Memorial Drive, Rochester, NY 14623, USA*

[6] *Space Telescope Science Institute, 3700 San Martin Dr., Baltimore, MD 21218, USA*

[7] *Department of Physics and Astronomy, University of California, 900 University Ave, Riverside, CA 92521, USA*

[8] *University of Massachusetts Amherst, 710 North Pleasant Street, Amherst, MA 01003-9305, USA*

[9] *National Astronomical Observatory of Japan, 2-21-1 Osawa, Mitaka, Tokyo 181-8588, Japan*

[10] *Gemini Observatory/NSF's National Optical-Infrared Astronomy Research Laboratory, 950 N. Cherry Ave., Tucson, AZ 85719, USA*

[11] *Instituto de Astrofísica de Canarias, La Laguna, Tenerife, Spain*

[12] *Universidad de la Laguna, La Laguna, Tenerife, Spain*

[13] *Université Paris-Cité, LERMA - Observatoire de Paris, PSL, Paris, France*

[14] *NSF's National Optical-Infrared Astronomy Research Laboratory, 950 N. Cherry Ave., Tucson, AZ 85719, USA*

[15] *Department of Physics and Astronomy, Texas A&M University, College Station, TX, 77843-4242 USA*

[16] *George P. and Cynthia Woods Mitchell Institute for Fundamental Physics and Astronomy, Texas A&M University, College Station, TX, 77843-4242 USA*

[17] *ESA/AURA Space Telescope Science Institute*

[18] *Astrophysics Science Division, NASA Goddard Space Flight Center, 8800 Greenbelt Rd, Greenbelt, MD 20771, USA*

[19] *Department of Physics, 196A Auditorium Road, Unit 3046, University of Connecticut, Storrs, CT 06269, USA*

[20] *Department of Astronomy, University of Michigan, 1085 S. University Ave, Ann Arbor, MI 48109-1107, USA*

[21] *INAF Osservatorio Astronomico di Roma, Via Frascati 33, 00078 Monteporzio Catone, Rome, Italy*

[22] *CEA, IRFU, DAp, AIM, Université Paris-Saclay, Université Paris Cité, Sorbonne Paris Cité, CNRS, 91191 Gif-sur-Yvette, France*

[23] *Department of Physics & Astronomy, University of California, Irvine, 4129 Reines Hall, Irvine, CA 92697, USA*

[24] *Centro de Astrobiología (CSIC-INTA), Ctra de Ajalvir km 4, Torrejón de Ardoz, 28850, Madrid, Spain*

[25] *Centre for Astrophysics & Supercomputing, Swinburne University of Technology, Hawthorn, VIC 3122, Australia*

[26] *ARC Centre of Excellence for All Sky Astrophysics in 3 Dimensions (ASTRO 3D)*

[27] *Department of Physics, 196 Auditorium Road, Unit 3046, University of Connecticut, Storrs, CT 06269, USA*

[28] *Department of Physics and Astronomy, University of California, Riverside, CA 92521, USA*

[29] *Racah Institute of Physics, The Hebrew University of Jerusalem, Jerusalem 91904, Israel*

[30] *Physics & Astronomy Department, University of Louisville, 40292 KY, Louisville, USA*

[31] *Columbia Astrophysics Laboratory, Columbia University, 550 West 120th Street, New York, NY 10027, USA*

[32] *Centro de Astrobiología (CAB), CSIC-INTA, Ctra. de Ajalvir km 4, Torrejón de Ardoz, E-28850, Madrid, Spain*

[33] *Department of Physics and Astronomy, Johns Hopkins University, 3400 N. Charles Street, Baltimore, MD 21218, USA*